PHYSICAL REVIEW B VOLUME 59, NUMBER 5 1 FEBRUARY 1999-I

Defects in liquid selenium

G. Kresse,* F. Kirchhoff,† and M. J. Gillan
Department of Physics, Keele University, Staffordshire ST5 5BG, United Kingdom

(Received 9 April 1998)

We use the data generated in recent first-principles molecular-dynamics simulations of liquid selenium at the temperatures 570, 870, and 1370 K to investigate defects in the liquid. The defects represent disruptions of the chain structure associated with onefold and threefold atoms (C_1 and C_3 defects). We stress that for a full understanding we need to analyze the defects from the viewpoints of atomic coordination, defect dynamics, and electronic structure, and we develop analysis techniques to do this. We find that localized electronic states at the top of the valence band and the bottom of the conduction band are associated with C_1 and C_3 defects, respectively. At 570 K, the concentration of defects is very low, and they exist as C_1 and C_3 defects in bound pairs (intimate valence-alternation pairs), but at high temperatures the defects are isolated and are mainly of C_1 type. The defect concentrations are used to determine the mean length of Se chains, which we find to be much smaller than the values deduced from NMR measurements at lower temperatures, but in reasonable agreement at 1370 K. Analysis of the defect dynamics shows that the residence time of defects on individual atoms becomes extremely short—comparable with the vibrational period—at high temperature.
[S0163-1829(99)05105-X]

I. INTRODUCTION

We have recently reported a detailed study of liquid selenium (*l*-Se) over a range of temperatures, using first-principles molecular-dynamics simulation (FPMD) (Ref. 1, referred to hereafter as paper I). We showed that the simulations reproduce fairly accurately the measured structural properties of *l*-Se, as characterized by the structure factor $S(k)$ and the pair-correlation function $g(r)$, and give a good account of dynamical properties, including the self-diffusion coefficient and the vibrational spectrum. Our results agreed with experiment in showing that the electronic structure of Se changes little on melting. The simulations were also analyzed to yield information that is hard to derive from experiment, such as the bond-angle distribution and the concentration and structure of Se_n rings in the liquid. However, there was an important question that was not addressed in paper I: the nature of defects in *l*-Se. This is the subject of the present paper.

For most liquids, it would make no sense to discuss defects, but for *l*-Se the defect concept has played a central role in both the experimental and theoretical literature. The concept makes sense in *l*-Se because of the chain structure of the liquid. The trigonal form of crystalline Se (*t*-Se, the stable structure under ambient conditions) consists of a regular array of infinite chains aligned along the trigonal axis. It is generally accepted that this chain structure survives almost intact on melting ($T_m = 490$ K), one indication of this being the exceptionally high viscosity of the melt.[2,3] Diffraction measurements show that the atomic coordination number is almost exactly 2 in the low-temperature liquid,[4–9] and remains close to 2 (Refs. 8–10) up to the critical point ($T_c = 1860$ K, $p_c = 380$ bar).[11,12] However, the viscosity drops rapidly with increasing *T*, and at $T \simeq 1000$ K it is similar to that of normal metals like Na.[3] The interpretation is that the perfect chain structure becomes progressively disrupted as *T* increases, so that there are increasing numbers of onefold (1F) and three-fold (3F) coordinated atoms—but with the *average* coordination staying close to 2. The chains become shorter, and the atoms move around more easily. It is natural to regard the localized disruptions of the perfect structure as defects. Particularly at low temperatures, where the disruption is slight and the defect concentration low, the defects should be very well defined.

Defects also give a natural way of thinking about the electronic properties of *l*-Se. If the perfect chain structure is preserved on melting, the electronic structure would be expected to change little. This is what happens initially: at low temperature ($T < 600$ K), the liquid is a wide-gap semiconductor, with an optical gap of around 2 eV (Refs. 8 and 13) (the optical gap in *t*-Se and amorphous Se are 1.9 eV and approximately 2 eV,[8] respectively), and a temperature-independent diamagnetic susceptibility.[14–17] However, with increasing temperature, the liquid becomes paramagnetic, and electron-spin-resonance (ESR) signals[18] and nuclear magnetic resonance (NMR) shifts[17] have been observed above $T \sim 600$ K. The paramagnetic susceptibility increases along the liquid-vapor coexistence line up to the critical point, and the optical gap decreases (to ~ 1.0 eV at 1173 K).[13] The electrical conductivity increases with temperature up to 1500 K,[19] as would be expected for a semiconductor, but beyond this point the conductivity drops, and the system becomes an insulator at the critical point.[19] A modest increase of pressure from the critical point causes the optical gap to close,[20,21] the conductivity to increase to semimetallic values, and the paramagnetic susceptibility to fall—the latter behavior has been associated with a change from Curie to Pauli paramagnetism.[17] The various regimes of behavior we have mentioned are summarized in the pressure-temperature diagram shown in Fig. 1.

In the semiconducting paramagnetic regime, there clearly must be free-electron spins, and it is natural to associate these with the coordination defects. For example, a 1F atom represents the end of a chain formed by breaking a covalent

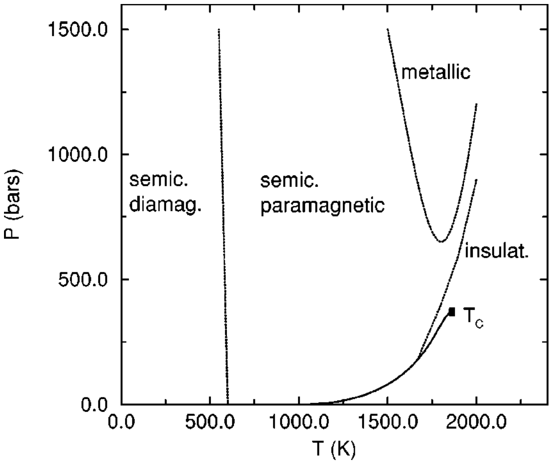

FIG. 1. Schematic pressure-temperature diagram of *l*-Se showing the four regimes discussed in the text. The full line indicates the liquid-vapor coexistence line (taken from Ref. 11). The boundaries between the regimes are only approximate. T_c marks the critical point.

bond, and a free spin occupying a state in the band gap is commonly associated with a dangling bond. This connection between free spins and chain ends is the leading idea in the classic study of Warren and Dupree[17], in which NMR techniques were used to estimate the concentration of defects, and hence the length of chains in *l*-Se as a function of temperature. However, a more detailed picture of the electronic structure of the defects has remained elusive. There is an often quoted theory of the low-temperature diamagnetic state due to Kastner, Adler, and Fritzsche,[22–24] according to which the most stable defects are 1F negatively charged and 3F positively charged defects, denoted C_1^- and C_3^+, respectively. These are called valence-alternation pairs (VAP's), because they are believed to occur in roughly equal numbers. It has also been proposed that bound C_1^--C_3^+ pairs may be energetically stable, and these have been called intimate VAP's, or iVAP's. Because the defect states involved are either doubly occupied or unoccupied, these defects do not carry net spins. This explains why the low-temperature material is diamagnetic, even though significant defect concentrations have been observed in photoluminescence[25] and photoinduced ESR.[26] The paramagnetic behavior at medium temperatures (Fig. 1) is presumed to arise from the electronic excitation of C_1^- and C_3^+ defects to form neutral C_1^0 and C_3^0 defects carrying net spins, with the C_1^0 defects (i.e., dangling bonds at chain ends) being dominant. However, this remains speculative.

It is evident from what we have said that in order to understand the defects in *l*-Se we need a clear picture of them from three points of view: their coordination (how the atoms are arranged); their dynamics (how the defects are created and destroyed and how they move through the system); and their electronic structure (energies and spatial localization of the defect electronic states). FPMD is uniquely placed to contribute, since it gives a completely unified electronic and statistical-mechanical description of the system in thermal equilibrium. Since our FPMD simulations reported in paper I reproduce the known properties of *l*-Se rather well, we expect that they will give an accurate picture of the three-dimensional structure of the liquid, and will allow us to analyze the coordination and dynamical aspects of the defects, and their equilibrium concentration—and hence the temperature-dependent chain length. We shall also use the simulations to investigate the electronic structure of the defects, though here we have to recognize that the single-electron Kohn-Sham states calculated in the FPMD are not the same as the experimental quasiparticle states, so caution is needed in interpreting the electronic structure.

For all calculations presented in this paper we have used the plane-wave pseudopotential package VASP (Refs. 27 and 28) (Vienna *ab initio* simulation package; for more details on pseudopotential parameters, etc., we refer to paper I). Generalized gradient corrections according to Perdew and Wang (commonly referred to as PW91)[29] were included in all calculations. We have shown in paper I that these corrections are essential for an accurate description of the weak interaction between chains in *t*-Se and *l*-Se. The simulations on which the present work is based were performed on a periodically repeated system of 69 atoms.

In the following sections, we use the data for time-dependent atomic positions and Kohn-Sham states generated in our three simulations at 570, 870, and 1370 K to analyze the properties of the defects. These three temperatures correspond roughly to the diamagnetic (570 K), paramagnetic (870 K), and transition (1370 K) regimes. We want to stress here that our molecular-dynamics simulations and all the calculations presented here have been performed with non-spin-polarized density-functional theory. Because unpaired electrons have not been considered, paramagnetism is precluded in the present calculations. We shall argue later that this should not affect the general validity of the picture developed for the electronic properties of the defects, but clearly it is a significant limitation which will need to be borne in mind when interpreting our results. Our aims will include the identification of the different kinds of defects and the calculation of their concentrations as a function of temperature; the characterization of the defects in terms of the local electronic density of states; the analysis of the defect dynamics, focusing particularly on the mean residence time of defects on atoms; and the interpretation of the total electronic density of states, particularly in the region of the band gap, in terms of the defects.

A substantial part of the paper (Sec. II) will be devoted to developing the methodology needed to detect and analyze the defects, which we shall see is not at all trivial. Section III then reports results for the defect concentrations and chain length, and Sec. IV describes the defect dynamics. Section V relates the electronic structure of the defects to that of the system as a whole. Section VI summarizes the defect picture that emerges from our simulations, and attempts to relate this to experimental data and previous theoretical discussions. Our conclusions are given in Sec. VII

II. DEFECT CHARACTERIZATION

A. Coordination defects

The most obvious way to identify defects is through the coordination number of atoms. The concept here is that in the nondefective state the liquid consists of infinite chains, in which every atom is coordinated to two neighboring atoms.

TABLE I. Average numbers of defects (per 100 atoms) observed in our FPMD simulations (Ref. 1) at 870 K using the techniques of instantaneous and quenched coordination analysis and dynamical analysis (see Secs. II A and II B). For each analysis technique, results are given for cutoffs r_c of 2.90 and 2.82 Å. The table reports numbers of onefold- and threefold-coordinated atoms (f_1 and f_3), numbers of isolated C_1 and C_3 defects, and numbers of C_1-C_3 and C_3-C_3 nearest-neighbor pairs.

	Instantaneous		Quenched		Dynamic	
r_c(Å)	2.90	2.82	2.90	2.82	2.90	2.82
f_1	3.4	5.7	1.9	2.2	2.1	2.8
f_3	8.5	4.8	2.1	1.8	2.6	1.8
C_1	3.0	5.3	1.5	1.8	1.8	2.5
C_3	2.1	1.5	1.7	1.4	1.5	1.1
C_1-C_3	0.4	0.4	0.4	0.4	0.3	0.3
C_3-C_3	3.0	1.5	0	0	0.4	0.2

Then in the real system every atom whose coordination number differs from 2 is regarded as a coordination defect. In practice, almost all such defects will be associated with onefold- or threefold-coordinated atoms, and we call these C_1 and C_3 defects, respectively. In this scheme, the coordination number of an atom means the number of neighboring atoms within a chosen cutoff distance r_c of the atom. We will refer to defects defined in this way as instantaneous coordination defects.

Unfortunately, this scheme is not satisfactory as it stands, because it is too sensitive to the choice of r_c. To illustrate this, we report in Table I the fraction of 1F and 3F atoms found in our FPMD simulation of *l*-Se at 870 K for r_c chosen as 2.82 or 2.90 Å, both of these values being near the radius of the first minimum in the radial distribution function $g(r)$ (see paper I). The table also gives the fractions of isolated C_1 and C_3 defects, as well as of configurations C_3-C_1 in which a 3F atom and a 1F atom are within radius r_c of each other, and configurations C_3-C_3 consisting of neighboring 3F atoms. The table shows that the 2 very similar values of r_c give concentrations differing by as much as a factor of 2 for some configurations.

The sensitivity to r_c is not unexpected. Disorder in the system is due to both vibrations and defects. Vibrations alone can stretch bonds or cause unbonded atoms to approach each other so that coordination numbers change, and the changes are likely to be strongly affected by the choice of r_c. But here we are not interested in vibrations, and we must seek to remove coordination fluctuations due to vibrations. The simplest way to do this is by quenching: for any given configuration, we relax the system into its nearest local energy minimum. In practice, we perform this relaxation using a conjugate-gradient algorithm[30]. Quenching has the effect of removing vibrations entirely, so that our coordination analysis detects only genuine defects. To illustrate the effect of quenching, in Fig. 2 we show the pair-correlation function before and after quenching for one configuration from the simulation at 870 K. As expected, quenching causes a strong narrowing of the first and second peaks; more importantly, it leaves almost no neighbors in the region of the first minimum, so that there is a sharp distinction between first and second neighbors.

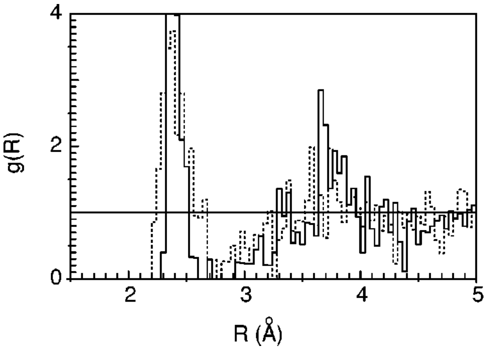

FIG. 2. The radial distribution function $g(r)$ for a single configuration from our FPMD simulation of *l*-Se at 870 K (dotted line) compared with $g(r)$ for the corresponding quenched configuration (full line).

For the following analysis we have quenched six selected configurations from our 570-K simulation, eight configurations from the 870-K simulation, and six configurations from the 1370-K simulation. At 870 K, quenching greatly improves the clarity of the defect analysis, as shown in Table I. The defect concentrations are now affected only a little by the choice of r_c. This confirms that the defects are real physical objects, whose existence does not depend much on their definition. Even so, decrease of r_c still increases slightly the number of 1F atoms and decreases slightly the number of 3F atoms, as would be expected. This means that the distinction between C_1 and C_3 defects is still not completely robust. Note though that the *total* number of coordination defects is almost completely unaffected by the small change of r_c.

In Fig. 3 we illustrate the geometry of the isolated defects C_1 and C_3 and the pairs C_3-C_1 and C_3-C_3 taken from typical quenched configurations. Detailed examination of the bond lengths shows that most of the C_3 defects exhibit a kind of ''Jahn-Teller distortion'' in which one of the bonds is considerably longer than the other two; this bond is colored white in Fig. 3. The long bond is responsible for the

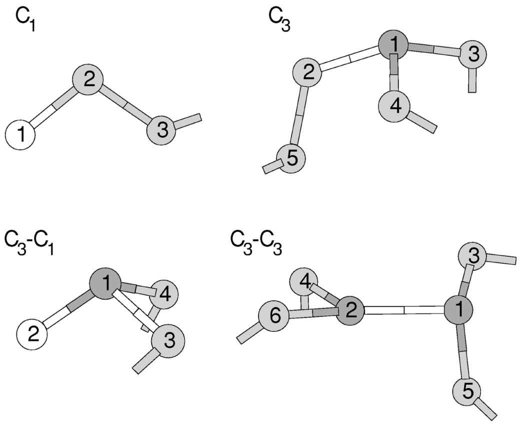

FIG. 3. Geometry of isolated C_1 and C_3 defects and C_3-C_1 and C_3-C_3 pairs from typical configurations quenched from our FPMD simulation at 870 K. White, midgray, and dark-gray spheres represent onefold-, twofold-, and threefold-coordinated atoms, respectively. The long bond usually associated with threefold atoms is colored white in the pictures of the C_3 defects.

TABLE II. All possible bond-breaking and -making events and the result of each event.

Event	Result of event
bond-making between $2F$ $2F$	creation of two C_3 defects
bond-breaking between $2F$ $2F$	creation of two C_1 defects
bond-breaking between $3F$ $2F$	defect hop $C_3 \rightarrow C_1$
bond-making between $2F$ $1F$	defect hop $C_1 \rightarrow C_3$
bond-making between $1F$ $1F$	annihilation of two C_1 defects
bond-breaking between $3F$ $3F$	annihilation of two C_3 defects

small peak in the gap between first and second neighbors in $g(r)$, which is visible in Fig. 2. This long bond is also responsible for the ambiguity in distinguishing between C_1 and C_3 defects pointed out above. We note from Table I the significant concentration of C_3-C_1 pairs (iVAP's in the terminology of Kastner, Adler, and Fritzsche[24]), and we return to this later. We also note the complete absence of C_3-C_3 pairs in the quenched coordination analysis, which indicates that their presence in the instantaneous analysis is solely due to vibrations. [By contrast, C_3-C_3 pairs were found, after quenching, by Hohl and Jones.[31] We believe the difference is due to the use of the generalized gradient approximation (GGA) rather than the local-density approximation (LDA) in our simulations. As shown in paper I, this improves the agreement with experiment, and increases the ratio between interchain and intrachain distances.]

B. Dynamical analysis

Because the physics presented in this paper depends so much on the clear identification of defects, we wanted to develop a second independent way of detecting defects which could be cross-checked against the quenched coordination analysis presented above. This second way makes use of the dynamics of defects. Since defects are defined through the coordination number of atoms, and since coordination numbers change by the making and breaking of bonds, these bond-making and -breaking events can be interpreted in terms of defect motions. For example, the breaking of a bond between two 2F atoms creates two C_1 defects; conversely, the making of a bond between two 1F atoms represents the mutual annihilation of two C_1 defects; the formation of a bond between 2F and 1F atoms means the hop of a C_1 defect on the atom that was initially 1F to form a C_3 defect on the atom that was initially 2F. Table II lists all possible events (assuming that there are only 1F, 2F, and 3F atoms) and their interpretation in terms of defect creation, annihilation, and hopping. Using these definitions, we can analyze our FPMD simulations to determine the nature of the defects and their locations at any instant.

In doing this analysis, the first step is to construct a list of all bond-making and -breaking events. For each such event, we record the time step at which the event occurred, the labels of the two atoms involved, and their coordination numbers before and after the event. The next step is to link together the events in the list. Suppose, for example, that at some time t_1 there is a bond-breaking event between the initially 2F atoms 1 and 2. Suppose further that the next event involving atom 1 is at time t_2, and involves a bond-making event between atom 1 and a 2F atom 3. The interpretation is that at t_1 two C_1 defects were created on atoms 1 and 2. The C_1 defect on atom 1 remained on this atom until t_2, at which instant it hopped to atom 3, being turned into a C_3 in the process. These defect processes deduced from the event list can be represented graphically (see Fig. 4). We represent each event by a dot on a time scale which we draw with time increasing downwards. The dots are connected by lines which represent the presence of a defect on a particular atom; we draw a C_1 defect as a continuous line and a C_3 defect as a broken line. In the above example, the bond break between atoms 1 and 2 is represented as a dot at time t_1. The continuous line representing the C_1 defect on atom 1 extends to time t_2, where it is terminated by a dot marking the bond-make between atoms 1 and 3. A broken line then extends downwards from this dot, showing the presence of the C_3 defect on atom 3. The C_1 defect on atom 2 created at t_1 is, of course, shown by a continuous line extending down from the dot at t_1. It is clear from this example that all dots are connected into chains. Dots representing defect creation join to two lines (both continuous or both broken) going to later times; those representing annihilation join to two lines (both continuous or both broken) coming from earlier times; and those representing defect hops join to two lines (one of each kind), one coming from earlier time and the other going to later time. If we analyze a simulation run having a given duration, some of these chains will be closed loops contained entirely within this duration; others will be open chains which begin and end at the beginning or end of the duration. To illustrate this scheme, in Fig. 4 we show the graphical representation of the defect events from a short section of the simulation at 870 K. At the start of this section, there are no defects; but a short way into the section, a pair of defects are created, which persist until the end of the section.

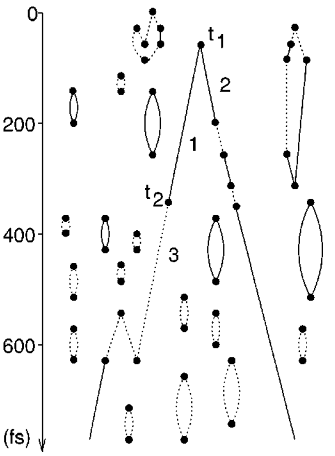

FIG. 4. Graphical representation of linked defect events from a short section of the FPMD simulation at 870 K. Time (units of fs) increases downward, full and dotted lines represent C_1 and C_3 defects residing on particular atoms, and dots show defect events.

Thus far, we have done nothing but represent the *instantaneous* coordination analysis of Sec. II A in a graphical manner. In particular, the defects present at any instant t (i.e., the continuous or broken lines intersected by a horizontal line drawn at time t) are precisely those revealed by that analysis. The crucial step in the dynamical analysis is now the removal of all closed loops which leave the connectivity of the atoms unchanged. The meaning of this step can be understood by noting that in a typical analysis, there are large numbers of closed loops containing just two events, as shown in Fig. 4. These loops can arise in two ways: either the bond between two 2F atoms becomes vibrationally stretched for a short time so that its length exceeds r_c, but the bond then recovers its normal length; or two 2F atoms approach each other for a short time so that their separation falls below r_c, but they then move apart again. These processes are exactly what we wish to ignore, since they arise from chain vibrations rather than from genuine defects. We therefore delete all two-dot loops. But there are also more complex loops which leave the connectivity unchanged; two examples are shown in Fig. 4. The general rule is that we delete all closed loops in which every bond-breaking event between a given pair of atoms is matched by a corresponding bond-making event between the same pair of atoms. We refer to these as ''redundant'' loops. The deletion of redundant loops leaves a set of irreducible graphs which we regard as representing the genuine defects.

We want to stress that the deletion step in the present dynamical analysis is expected to have much the same effect as quenching in the coordination analysis. The principle in both cases is that we wish to ignore fluctuations which leave unchanged the topological connections of the Se chains. We would therefore hope that the two kinds of analysis would identify essentially the same defects, and in particular would give the same numbers of defects in a given simulation. This is indeed what we find, as shown by the results of the dynamical analysis for the 870 K simulation which we report for two values of r_c in Table I. It is true that the concentrations of the different types of defect are not identical in the quenched and dynamic analysis, but they are sufficiently close to show that the two analysis are detecting essentially the same defects. This will be further confirmed when we discuss the temperature dependence of the defect concentrations in Sec. III.[32,33]

C. Electronic structure of defects

1. Local densities of states

We expect the defects revealed by our coordination and dynamical analysis techniques to give rise to localized electronic states. The tool we use to investigate the electronic structure of the defects is the electronic density of states (DOS). We focus here on the local density of states (LDOS), which tells us the density of electronic states in the region of a chosen atom. This is defined in terms of the number of electrons c_{ni} on atom i due to Kohn-Sham orbital $\psi_n(\mathbf{r})$, which is given by

$$c_{ni}=\int_{r<R_c} d\mathbf{r}|\psi_n(\mathbf{R}_i+\mathbf{r})|^2, \tag{1}$$

where $\mathbf{R}_i$ is the position of atom i, and the integration goes over a sphere of radius R_c centered on this atom. In practice, we choose R_c so that the volume of the sphere is equal to the mean volume per atom in the system. Then the LDOS on atom i, denoted by $n_i(E)$, is

$$n_i(E)=\sum_n c_{ni}\delta(E-E_n), \tag{2}$$

where E_n is the Kohn-Sham energy of orbital n, and the sum goes over all orbitals.

In Fig. 5 we show the average LDOS of nondefective atoms and of atoms associated with C_1 and C_3 defects and C_1-C_3 pairs. The energy range shown in the figure covers only the Se$(4p)$ states, since the Se$(4s)$ energy region contains nothing of interest. All the results refer to quenched configurations; those for nondefective atoms and for C_1-C_3 pairs are from our simulations at 570 K and the others from our simulations at 870 K.

In assessing the results, we use the nondefective LDOS [Fig. 5(a)] as our point of reference. This LDOS consists of three major peaks, and closely resembles the DOS of the trigonal crystal. The origin of these peaks has often been described (see, e.g., paper I). On each atom, two of the three p orbitals form bonding and antibonding combinations ($pp\sigma$ and $pp\sigma^*$) with two neighbors, and these states give rise to the lower and upper peaks in the DOS. The third p orbital does not participate in bonding and is associated with the middle peak. Since the pair of electrons in such a nonbonding orbital is often called a lone pair, the peak is labeled LP in the figure. Each of the major peaks is capable of holding two electrons per atom. With four p electrons per atom, the Fermi energy therefore falls into the band gap between the middle and upper peaks.

The LDOS for C_1 defects [Fig. 5(b)] shows marked differences from the reference nondefective LDOS. First, the weight of the nonbonding middle peak is increased, and that of the bonding and antibonding peaks is reduced. Second, a sharp peak has appeared at the top of the valence band, indicated by an arrow. More detailed analysis reveals that this peak is due to a *single* state localized in the region of the C_1 defect. The degree of localization can be characterized by the values of c_{ni} for the appropriate state n [see Eq. (1)]; we find that the sum of c_{ni} on the C_1 site and its neighbor is 0.4, so that the defect state is fairly well localized (complete localization would give a value of unity).

Figure 5(c) shows the average LDOS for a C_3 site and for the neighbor connected to it by the long bond (atom number 2 in Fig. 3). Compared with the nondefective LDOS, the nonbonding peak is now reduced and the bonding and antibonding peaks enhanced. In addition, there is a sharp peak at the bottom of the conduction band (arrowed), also visible in the LDOS of the long-bond neighbor. This state is rather strongly localized on the defect: the sum of c_{ni} on the C_3 atom and its long-bond neighbor is 0.4, and if the other two neighbors are included the sum rises to values of 0.6 – 0.7.

Finally, we note that the LDOS for C_1-C_3 pairs [Fig. 5(d)] shows the features of isolated C_1 and C_3 defects. However, we find only a single defect electronic state, which is at the bottom of the conduction band and is mainly localized on the C_3 site.

2. Interpretation of the density of states

We now give a brief interpretation of the LDOS for C_1 and C_3 defects and C_1-C_3 pairs [Fig. 5(b)–5(d)]. In a C_1 defect, a single p orbital on the 1F atom forms bonding and

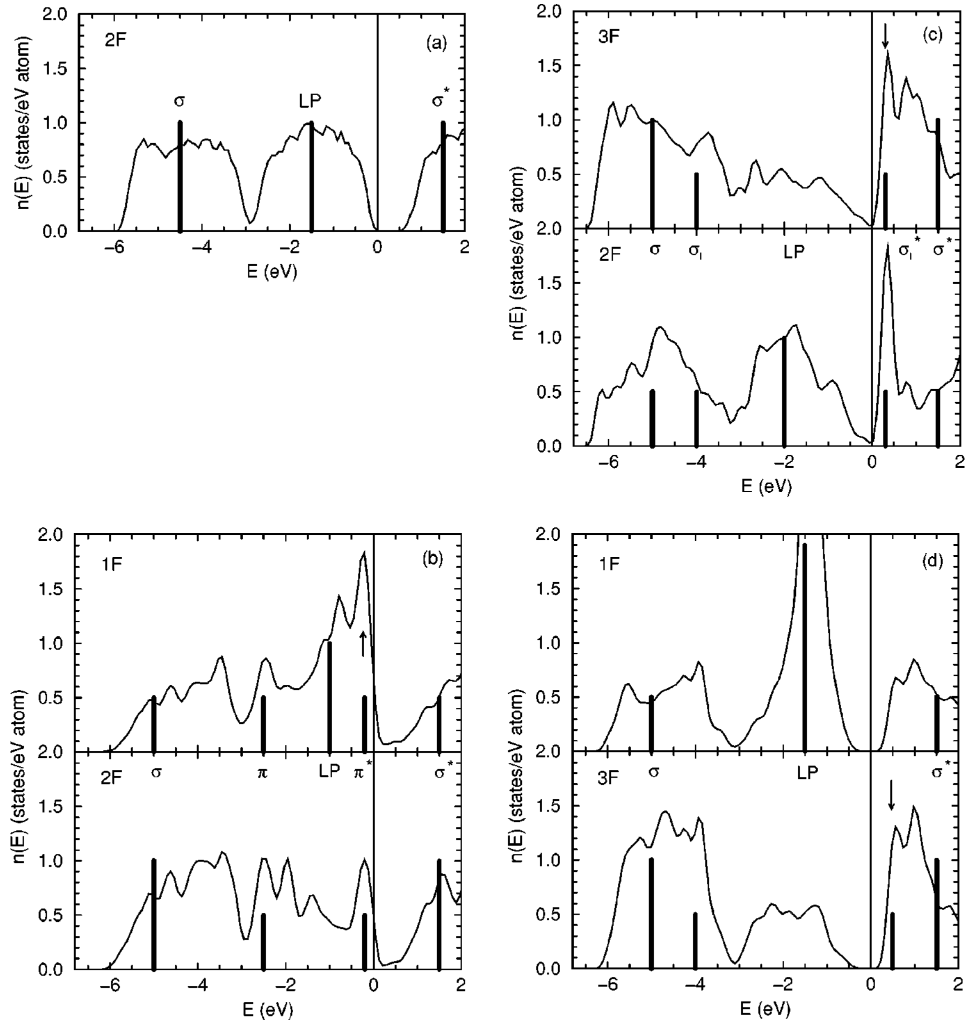

FIG. 5. Average local density of states (LDOS) for (a) nondefective twofold-coordinated atoms; (b) C_1 defects, (c) C_3 defects, and (d) C_1-C_3 defect pairs. Panels (b) and (c) show the LDOS both on the defect atom and on a neighboring 2F atom (see text). Panel (d) shows the LDOS on the 1F and 3F atoms of the defect pair. Solid bars show notional energies of combinations of atomic orbitals referred to in interpreting the LDOS, the length of the bar being proportional to the number of electrons per atom that can be held in the state (a length of 1 corresponding to two electrons).

antibonding states with the neighboring atom, and the other two p orbitals are nonbonding. The enhancement of the middle peak at the expense of the lower and upper peaks on the 1F site [Fig. 5(b)] is therefore expected. To understand the form of the middle peak, we need to note that one of the two nonbonding p orbitals on the 1F atom forms π bonds with the corresponding orbital on the neighbor, and this results in π and π^* subpeaks within the middle peak, as indicated in the figure. The sharp peak at the top of the valence band is the π^* state. Note that, compared with the nondefective DOS, the middle peak of the DOS for C_1 defects contains an additional state, which we can regard as being pulled down from the conduction band.

For C_3 defects [Fig. 5(c)], we have the opposite situation. All three p orbitals on the 3F atom now form bonding and antibonding combinations with neighbors, so that the middle peak in the LDOS loses weight to the upper and lower peaks. The σ-σ^* splitting is markedly smaller for the atoms in the long bond, and the associated states are marked σ_l and σ_l^* in the figure. The sharp peak at the bottom of the conduction band is associated with the σ_l^* state. Compared with the nondefective DOS, the valence band has lost a state to the conduction band, and we can identify this as the σ_l^* state.

Finally, for C_1-C_3 pairs [Fig. 5(d)], we see that the LDOS of the 3F site is similar to that of isolated C_3 defects, but the 1F LDOS differs from that of isolated C_1 defects in lacking the sharp peak at the top of the valence band. This can be understood by noting that the only neighbor of the 1F atom is the 3F atom. Since all three p orbitals on the latter are committed to σ bonds, no orbital is available to form a π bond with the 1F site, so the middle peak of the LDOS on this site is unusually narrow.

We turn now to the occupation numbers of the electronic defect states. If the numbers of C_1 and C_3 defects were equal, the Fermi level would fall near the middle of the gap, so that the C_1 defect state is doubly occupied and the C_3 state unoccupied. The C_1 and C_3 defects then carry one unit of negative and positive charge, respectively. This would correspond exactly to the VAP model of Kastner, Adler, and Fritzsche.[24] At 870 K, the numbers of the two defects are indeed comparable (see Table III), and for some times in our simulation they are exactly equal. In principle, we should be

TABLE III. Numbers of isolated C_1 and C_3 defects and C_1-C_3 nearest neighbors (per 100 atoms) obtained by quenched coordination analysis at three temperatures. Numbers in parentheses in the upper half of the table were obtained directly from quenched coordination analysis using a cutoff r_c of 2.9 Å. Numbers without parentheses were obtained by using defect electronic energies to discriminate between C_1 and C_3 (see Sec. II C 3). Results for the total number of defective atoms f_1+f_3 (per 100 atoms) were obtained from quenched coordination analysis and from dynamical analysis. Chain lengths ξ were obtained from Eq. (3).

	570 K	870 K	1370 K
C_1	0	2.1 (1.5)	7.2 (6.1)
C_3	0	1.1 (1.7)	1.4 (2.5)
C_1-C_3	1.4	0.4	0.7
f_1+f_3 (coordination)	2.8	4.0	10
f_1+f_3 (dynamical)	2.9	4.6	18
ξ	∞	62	23

able to detect the charges localized on the defects by integrating the appropriate LDOS up to the Fermi energy. In fact, when we do this, we do not find any significant electron transfer from C_3 to C_1. We believe there are two reasons for this. First, the spatial localization of the defect states is not very strong, as pointed out in Sec. II C 1. Second, electronic screening will tend to mask the transfer.

3. Electronic characterization of defects

We have seen that the coordination and dynamical analysis techniques do not distinguish very robustly between C_1 and C_3 defects (see Table I). In fact, the rapid interconversion of the defect types (see Fig. 4) means that the distinction is bound to be somewhat arbitrary. Nonetheless, the electronic structure gives us a convenient way of making it less arbitrary. To do this, we use our coordination analysis to locate the defects in the usual way. We then determine the defect electronic states in the gap region, and identify which defect each state belongs to. Our criterion is then that a defect is C_1 if its state is below the middle of the gap, and C_3 if it is above. It will be shown in Sec. III how this procedure is applied in practice.

III. DEFECT CONCENTRATION AND CHAIN LENGTH

We have used the simulation results reported in paper I to calculate the defect concentrations at the three temperatures 570, 870, and 1370 K. In Table III we report these concentrations, calculated using both the quenched coordination analysis (Sec. II A) and the dynamical analysis (Sec. II B). For the coordination analysis, the concentrations of C_1 and C_3 defects given in the table were calculated in two ways: first, by direct application of that analysis; and second by using the LDOS analysis (Sec. II C 3) to distinguish between C_1 and C_3.

Several important conclusions flow from Table III. First, we note that the *total* defect concentrations obtained from the quench analysis and the dynamical analysis are in close agreement at 570 and 870 K (the agreement is more approximate at 1370 K). This agreement between the two independent analysis schemes confirms that the defects that we are detecting are well defined and physically meaningful. We also note that the individual concentrations of C_1 and C_3 defects obtained by the quench analysis are altered significantly when we use the LDOS technique to distinguish between C_1 and C_3. This confirms that the atomic coordination is not enough by itself to give a robust characterization of the defects. (Note that, by definition, the *sum* of the C_1 and C_3 concentrations cannot be affected by the LDOS analysis.)

As expected, the results of Table III show that the total defect concentration increases rapidly with temperature. The close relation between this and the temperature dependence of the chain length, and dynamical properties such as the diffusion coefficient, will become clear later. We note that the C_1 concentration increases much more strongly than the C_3 concentration, the latter remaining very low even at 1370 K.

A further conclusion from Table III is that the defect concentration at 570 K arises from just a single C_3-C_1 pair in our simulation. On closer examination, we have found that at this temperature the list of neighbors in quenched configurations remains unchanged over several ps, so that the C_3-C_1 pair is effectively immobile. This is completely consistent with the very small diffusion coefficient at 570 K reported in paper I. The indication is that the major defects in the 570 K system are C_3-C_1 iVAP's at low concentration. To test this, we have generated a completely independent 570 K configuration by starting from the final configuration of our simulation at 870 K and cooling this slowly (over a 5-ps period) to 570 K; we then quench to zero temperature. As before, the resulting configuration contains just a single iVAP. We stress that the final configuration of the 870 K simulation did not contain a C_3-C_1 pair initially; the pair was created during the cooling and equilibration. This confirms the dominance of iVAP's in the low-temperature liquid. Our conclusion disagrees with the simulation results of Hohl and Jones[31] on low-temperature *l*-Se, which gave a much higher defect concentration than ours, and no dominance of iVAP's.

Finally, we note that, since the defect concentrations are small, especially at 570 and 870 K, they are inevitably subject to large fluctuations, and therefore significant statistical errors, in our simulated system of only 69 atoms. For example, in our simulation at 870 K, whose duration was 18 ps, the average 4.6% of defective atoms comes from a value which fluctuates with time between values of 0% and 7.2%; for a time of 2 ps during the simulation, there were actually no defects at all.

Our defect concentrations allow us to deduce the average length of Se chains. We stress that the chain length is not a uniquely defined quantity. In order to adopt a definition, we say that C_1 and C_3 defects both represent the end of *one* chain. In this definition only the long bond of a C_3 defect (the white bond between atom 1 and atom 2 in Fig. 3) is considered as a disruption of a chain, and C_1 and C_3 defects are treated on the same footing. A chain is then an unbroken sequence of twofold and threefold-coordinated atoms extending between two chain ends, and the length of the chain is the number of atoms it contains, including the atoms at its two ends. In this scheme, we ignore C_3-C_1 iVAP's. Then, ignoring also closed loops, the mean chain length ξ is given by

$$\xi = 2N_{\rm at}/(N_1+N_3), \tag{3}$$

where $N_{\rm at}$ is the total number of atoms in the system, and N_1 and N_3 are the mean numbers of C_1 and C_3 defects. (The question of closed loops was discussed in paper I, where we showed that their concentration is very small.)

From this chain analysis, our defect concentrations give the mean chain lengths reported in Table III. The values reported here are significantly larger than the very rough estimates reported in paper I. The reason is that we have removed the effects of thermal vibration in the present analysis. Our ξ values will be further discussed in Sec. VI.

IV. DYNAMICS OF DEFECTS

In discussing the dynamics of defects, the quantity we wish to emphasize is the defect residence time τ_r, by which we mean the average time that a C_1 or C_3 defect remains on a given atom. The reason why τ_r is important is that, as we shall see, it is intimately related to the mean bond lifetime τ_b and the self-diffusion coefficient *D*, which were discussed in paper I.

The first thing to consider is how to define τ_r. At first sight, it seems straightforward to define it in terms of our dynamical analysis (Sec. II B). In the graphical representation, a defect on an atom appears as a continuous or broken line joining two events, and the residence time is the duration of the line. It might seem from this that τ_r is simply the mean duration of the defect lines. However, a moment's thought shows that we face the same kind of issue as we did when defining the defect concentration, namely, the need to distinguish between true defect jumps and vibrational fluctuations. To see the problem, consider a free chain end (i.e., a C_1 defect). Vibrations may cause the atom 1 at the chain end to approach an atom 2 in another chain and then immediately move away again. In our dynamical scheme, the C_1 defect on 1 would be transformed fleetingly into a C_3 defect on 2, and then return to C_1 on 1. In order to capture the defect dynamics responsible for the bond lifetime and self-diffusion coefficient, we need to suppress this kind of rapidly reversed events due to vibrational fluctuations.

We suppress the unwanted events by essentially the same argument as we used in Sec. II B. Starting from the irreducible graphs defined there, we delete every bond-breaking or -making event between a pair of atoms if it is matched by the reverse bond-making or -breaking event between that pair—we refer to these as ‘‘canceling events.’’ The remaining events which survive this deletion are the ‘‘permanent’’ events used in calculating the residence time. We denote the number of permanent events per atom per unit time by n_b.

There is a direct relation between n_b, τ_r, and the total defect concentration *c* (number of all defects per atom). To see this, note that the residence of a defect on a given atom begins and ends with bond-making and -breaking events, so that the residence is associated with two events. The defect concentration is therefore given by

$$c = n_b \tau_r . \tag{4}$$

Since we already know *c*, we can calculate τ_r from n_b. The resulting values of τ_r are reported in Table IV. As noted in Sec. III, our 570-K simulation contained only a single C_3-C_1 pair, which was effectively immobile. This is confirmed by the dynamical analysis, which gave no uncanceled event pairs at all, so that τ_r is infinite within the accuracy of our calculations.

TABLE IV. Number of bond-breaking and -making events n_b per atom per ps, bond lifetime τ_b deduced from the number of bond-breaking events (values in parentheses report the results of paper I), and the residence time τ_r deduced by combining the defect concentration *c* (dynamical defect analysis) and the bond lifetime τ_b [see Eqs. (4) and (5)].

	570 K	870 K	1370 K
n_b (ps^{-1})	0	0.10	0.75
τ_b (ps)	∞ ($>$200)	20.0 (20.0)	2.7 (3.0)
τ_r (ps)	∞	0.46	0.24

The validity of this residence-time analysis can be corroborated by noting that it also gives a prediction for the bond lifetime τ_b, which can be checked against the values reported in paper I. (This is a useful check, since those previous values were obtained from a completely independent correlation-function analysis.) The mean numbers of bond-breaking and -making events per unit time must be equal, so that each must be equal to $\frac{1}{2}n_b$. We should therefore expect the bond lifetime to be given by

$$\tau_b = 2/n_b . \tag{5}$$

In Table IV, we compare the values of τ_b obtained from this equation with our previous values. The very close agreement confirms that the present analysis is well founded.

Our results for τ_r therefore establish a close relation between τ_r, τ_b, and the defect concentration *c*; this relation, and the connection with *D*, will be discussed further in Sec. VI. A striking feature of our results is that τ_r becomes extremely small at high temperatures: the value of 0.2 ps at 1370 K is only a few times the typical vibrational frequency. These values will be discussed further in Sec. VI.

V. TEMPERATURE-DEPENDENT ELECTRONIC PROPERTIES

We now examine the influence of the defects on the electronic properties of the liquid. In particular, we want to demonstrate the presence of spatially localized states in the band gap. As before, we must caution that this discussion is based on the Kohn-Sham single-particle energies, so that a direct comparison with experiment is not possible. Since the Kohn-Sham band gap is so much smaller than the experimentally accessible quasiparticle band gap, the information that we can obtain about the electronic gap states is inevitably rather qualitative.

In Figs. 6–8 we show the average electronic DOS for both unquenched and quenched configurations from our simulations at 570, 870, and 1370 K. To improve legibility, the DOS is broadened using a Gaussian of width 0.05 eV. Note that the unquenched DOS is essentially the same as what we already reported in paper I, but we show the results again in order to compare with the quenched DOS. Also shown in Figs. 6–8 is the participation ratio of the electronic states, which characterizes their degree of localization. In

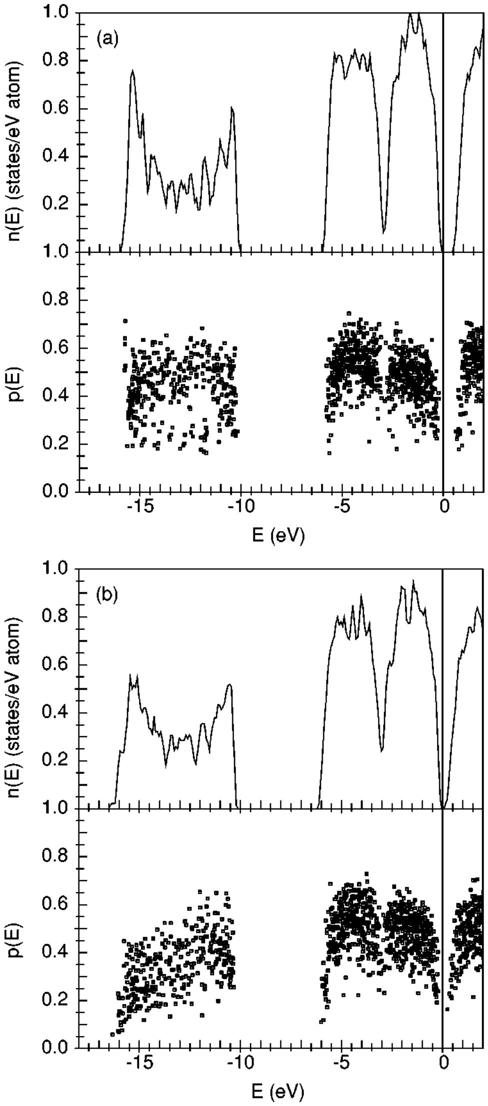

FIG. 6. Density of states $n(E)$ and participation ratio $p(E)$ for l-Se at 570 K. Panels (a) and (b) show results for quenched and unquenched configurations, respectively. The DOS has been convoluted with a Gaussian of width 0.05 eV.

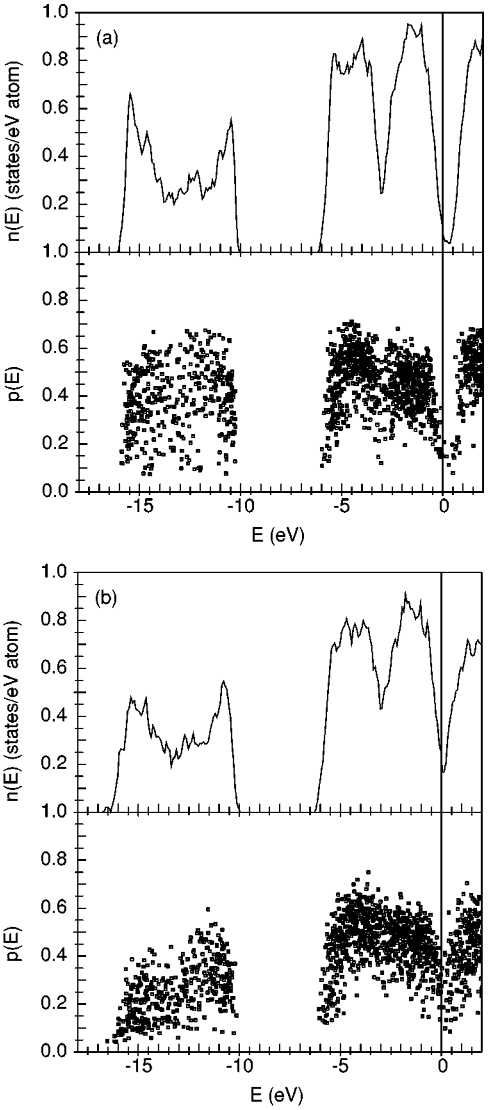

FIG. 7. Density of states $n(E)$ and participation ratio $p(E)$ for l-Se at 870 K. Panels (a) and (b) show results for quenched and unquenched configurations, respectively.

terms of the local electron numbers c_{ni} [see Eq. (1)], the participation ratio p_n of orbital n is defined as

$$p_n = \left(\sum_i c_{ni} \right)^2 \Bigg/ N_{\text{at}} \sum_i c_{ni}^2, \tag{6}$$

where the sums go over all N_{at} atoms in the system. The definition implies that p_n is of order unity for extended states and of order $1/N_{\text{at}}$ for states localized on a single atom. In addition to the DOS and the participation ratio, in Fig. 9 we show the time variation of the Kohn-Sham energies of states in the gap region.

Figure 6 shows that at 570 K the gap in the quenched system is approximately 1 eV, which is very similar to the gap calculated for crystalline Se using LDA and GGA.[34] The gap in the unquenched system is considerably smaller (~0.3 eV). Since the difference between the unquenched and quenched systems can be attributed to vibrations, this indicates that the reduction of the gap is due to vibrationally induced band broadening and band tailing. The small values of the participation ratio in the gap indicate localized states at the edges of the conduction and valence bands. More detailed examination shows that the states at the conduction-band edge are localized at the iVAP which we know to be present in our 570-K simulation (see Sec. III), whereas localization of the states at the valence-band edge is weaker, and no clear spatial localization of these states at the iVAP is discernible. Figure 9 shows a large energy fluctuation of the localized states at the conduction-band edge, and it is clear that the conduction-band tailing can be mainly attributed to this fluctuation. Interestingly our findings concerning band tailing resemble the situation found by Drabold *et al.* in amorphous Si.[35] In Ref. 35 the large fluctuations of the states at the conduction-band edge were explained by the large degree of spatial localization of these states: small distortions around the defect site will naturally result in large fluctuations of the corresponding eigenvalues. It seems plausible that the same conclusion holds for l-Se.

The DOS at 870 K (Fig. 7) shows that there are now states throughout the band gap in the quenched system. The small values of the participation ratio show that these are

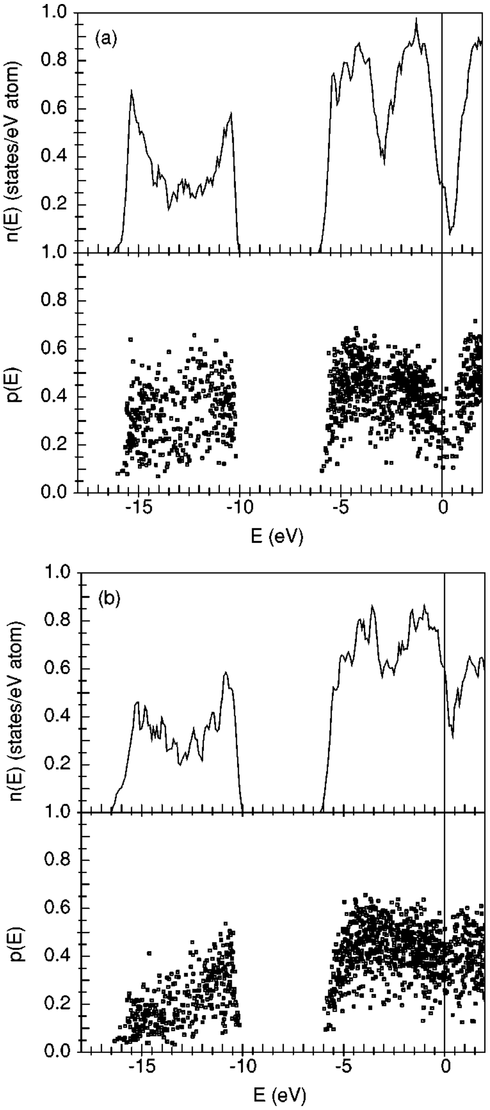

FIG. 8. Density of states $n(E)$ and participation ratio $p(E)$ for *l*-Se at 1370 K. Panels (a) and (b) show results for quenched and unquenched configurations, respectively.

localized and that a mobility gap within the pseudogap has formed. The band gap is significantly washed out in the unquenched system. We have seen already (Sec. III) that at 870 K iVAP's have been destroyed by thermal motion, and the dominant defects are C_1 and C_3 defects, with the former being more abundant. It is natural to associate the gap states with these defects. The graph of time-dependent Kohn-Sham energies (Fig. 9) is particularly instructive here. This shows extremely large fluctuations in the gap region, and reveals states which move across the full width of the gap. This is exactly what would be expected from our analysis of the localized states associated with C_1 and C_3 defects. We showed in Sec. II C 1 that these defects produce localized states at the top of the valence band and the bottom of the conduction band, respectively; we also saw in Sec. IV that C_1 and C_3 defects interconvert rapidly. Before leaving the 870-K simulation, we note one more significant feature in the DOS, namely, the small downward shift of the Fermi energy E_F with respect to the top of the valence band. This appears to be a direct consequence of the fact that there are more C_1 than C_3 defects.

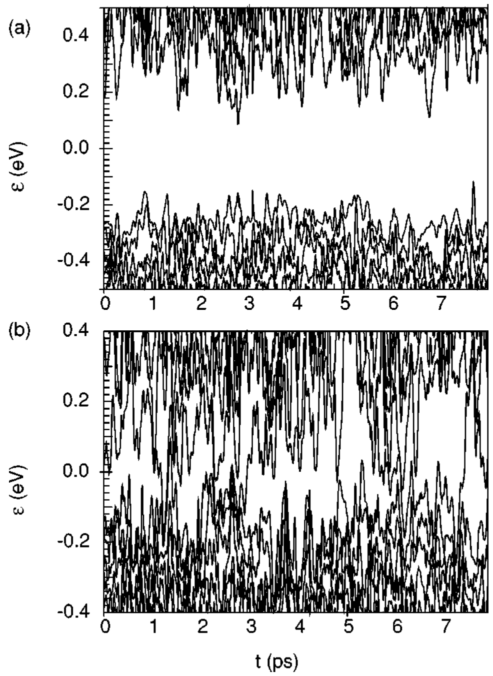

FIG. 9. Time evolution of Kohn-Sham single-particle energies in FPMD simulations at (a) 570 K and (b) 870 K. The energy zero is at the Fermi energy.

The DOS and participation ratio at 1370 K continue the trends seen on going from 570 to 870 K. The band gap becomes still further filled with states, some of which are strongly localized in the quenched system, and E_F moves further down into the top of the valence band.

In concluding this section, we emphasize again the two distinct reasons why increasing temperature causes the band gap to close. The first is the increase in the number of C_1 and C_3 defects and the spatially localized gap states associated with them. The second is the vibration-induced fluctuations of electron energies, which are particularly large for localized gap states, but also produce a general broadening of the bands.

VI. DISCUSSION

We have demonstrated that coordination defects can be clearly and (almost) unambiguously detected in our FPMD simulations, and that these are associated with 1F and 3F atoms. An extremely important feature of our demonstration is that it rests on two independent methods of analysis, based on quenching and on dynamics, which give almost the same numbers of defects of each kind at the three temperatures examined. We have also shown that the C_1 and C_3 defects are associated with spatially localized electronic states at the bottom and top of the band gap, respectively, and we have used the energies of these states to help discriminate between C_1 and C_3.

A key conclusion from our dynamical analysis is that C_1 and C_3 interconvert rapidly. Indeed, the analysis shows that the motion of the defects occurs precisely through this interconversion. This makes a strong case for saying that instead of different kinds of defects, C_1 and C_3, there are simply *defects*, each of which fluctuates in character between

C_1-like and C_3-like. The implication of this is that we should find the energy of the electronic defect state associated with each defect swinging back and forth across the gap as its character fluctuates. As discussed in Sec. V, this is exactly what we observe (see particularly Fig. 9).

We have shown that the concentration of defects increases rapidly with temperature, as expected from the increase of diffusion coefficient (see paper I) and decrease of viscosity. At the low temperature of 570 K, we have found that the only defects in our simulated system consist of a single C_3-C_1 pair combined to form an iVAP. This provides support for the model of Kastner, Adler, and Fritzsche. However, this support is not completely robust, because we find the defects to be immobile over many ps, so that there must be doubt whether our system is fully equilibrated with respect to defect concentration. We note that the earlier FPMD simulations of Hohl and Jones found no evidence that iVAP's are the dominant low temperature defects. However, their simulations were much shorter than ours, were based on a less accurate pseudopotential, and used the LDA, which we now know to be problematic for solid and liquid Se (see paper I); we therefore believe that their lack of evidence for iVAP's may not be significant.

For our simulations at 870 and 1370 K, equilibration is no longer a serious problem, so that our defect concentrations should be reliable—though we have noted the large fluctuations in these concentrations at 870 K, so our statistical accuracy may not be very high. Our finding is that at these temperatures iVAP's are no longer significant, and the defects are mainly isolated. The defect concentration is much larger than derived by Warren and Dupree[17] from NMR experiments. Unfortunately with 60 atoms in the chain, we already approach the number of atoms in the cell. This means that the average chain length and the defect concentration might be affected strongly by system size effects, which explains part of the discrepancies between our results and the values derived from NMR experiments.[17] However, another point might also play a significant role. At the intermediate temperature of 870 K, the concentrations of C_1 and C_3 defects are similar. This means that the Fermi energy falls between the two types of defect state, so that most of the defect electronic states are completely full (C_1^-) or completely empty (C_3^+). The implication might be that only a fraction of the defect states are paramagnetic centers, which is not consistent with the current interpretation of the NMR experiments given by Warren and Dupree.[17] Because our defect analysis was based on non-spin-polarized calculations, the description of unpaired electrons remains approximate. This limitation of our calculations is significant, since we do not allow for the unpaired spins observed in NMR experiments. In an attempt to gain some insight into this question, we have performed fully spin-polarized calculations for 12 configurations from the 870-K run. Most of these configurations contained two defects, some even more. But only three configurations resulted in an electronic ground state with unpaired electrons and a finite spin-polarization density. The one electron energies of those eigenstates that were affected by the spin polarization changed only by approximately 50–100 meV; or in other words, in the spin-polarized calculation, unpaired electrons gained an additional energy of 50–100 meV. Because this additional energy gain was accompanied by an energy change of other eigenstates, the influence on the total energy and the forces was even smaller (<10 meV and <0.05 meV/Å, respectively). The spin-polarized calculation implies that only those defect states which lie within an interval of 50–100 meV around the Fermi-level can be paramagnetic centers, for the 69-atom system only approximately one out of ten defects was a paramagnetic center. However, finite-size effects might affect these results as well, since it is known that the spatial localization of electronic defect states depends on the size of the system, and the degree of localization determines to a large extent the additional energy gained by unpaired electrons.

At the highest temperature of 1370 K, the concentration of C_1 defects becomes much greater than that of C_3 defects, or more accurately the defects spend the majority of their time in the C_1 state. This results in a shift of the Fermi level toward the valence-band edge. In our simulations, the band gap in the Kohn-Sham energy spectrum closes at around 1370 K, the mobility gap is very much weakened, and the eigenstates become extended. The main reason for the closure of the gap is the presence of large fluctuations in the eigenvalues induced by thermal vibrations. Although the closing of the gap happens at a significantly lower temperature than in the experiment, we believe that the process responsible for the transition to the metallic regime in the real liquid is similar to what we observe.

The chain lengths ξ deduced from our defect concentrations are 62 and 23 at 870 and 1370 K, respectively. The value at 870 K is very much lower than the experimental estimate of ~ 1000 reported by Warren and Dupree.[17] From Fig. 7 of their paper, we estimate that our ξ is lower than theirs by about a factor 15 at 870 K, though the agreement looks good at 1370 K. We have already noted that the discrepancies could be due either to finite-size effects or to the fact that only a small fraction of the coordination defects are paramagnetic centers. As we shall now show, an interesting constraint on ξ can be obtained by considering the defect dynamics.

We have stressed the close relation between the defect residence time τ_r, the bond lifetime τ_b, and the diffusion constant D. The relation between τ_r and τ_b can be summarized by combining Eqs. (4) and (5) to give $c = 2\tau_r/\tau_b$, where c is the defect concentration. The relation between τ_b and D was discussed in paper I, and can be expressed in terms of the root-mean-square distance R_0 that an atom diffuses every time one of the bonds connecting it to a neighbor is broken. The relation is $R_0^2 = 6D\tau_b$. One would expect R_0 to be on the order of the nearest-neighbor distance in the liquid, and the value obtained in paper I was $R_0 \simeq 5$ Å, i.e., about twice the radius of the first peak in $g(r)$. Now we have every reason to believe that our simulation results for D are realistic: first, because they agree roughly with experimental values in the temperature range 523–723 K (see paper I); and second because at high temperature we find values typical of normal liquids like l-Na, as would be expected from the low viscosity of l-Se in this region. This means that our bond lifetimes should also be realistic. Given τ_b, then the relation $c = 2\tau_r/\tau_b$ puts a constraint on c. The reason is that the residence times τ_r given by our dynamical analysis (Table IV) are already remarkably short: at 870 K, τ_r is only 0.46 ps, which is only a few times the minimum vibrational period of ~0.1 ps; at 1370 K, τ_r is even shorter. It is difficult to conceive that τ_r could be *very* much shorter than this, because this would require the defects to move faster than the speed of sound, i.e., roughly the nearest-neighbor distance divided by the vibrational period. If these arguments are correct, the implication is that the defect concentration is unlikely to be much smaller than the values we have found, and the chain length is unlikely to be much greater. This strong disagreement with the much higher values of ξ reported by Warren and Dupree would be explained if only a small fraction of the coordination defects were paramagnetic centers, as we suggested above.

In concluding this discussion, we note some deficiencies in the present work, which we hope to repair in future work. We have noted several times the difficulties caused by having to rely on the Kohn-Sham energies to draw conclusions about the spectrum of electronic states. In principle, it should be possible to overcome this problem by calculating the quasiparticle energies *via* the GW approximation.[37] So far as we are aware, this has never been attempted for a liquid, but recent advances in GW techniques[38] should make it possible in the near future. Equally important are finite-size effects. At 570 and 870 K, the chains are so extended that system size effects might play an important role. Investigations are currently underway to clarify this point. Another deficiency is that we have not considered electron spin in the molecular dynamics and in most presented calculations. This means that the electronic states are constrained to be either doubly occupied or unoccupied. At 870 K, calculations for 12 selected configurations seem to imply that spin polarization will not have a significant influence on the forces and the structure. But we hope in the future to perform full spin-polarized FPMD calculations, as has already been done for *l*-Si[36]—which should allow us to investigate this question in more detail.

VII. CONCLUSIONS

Our main conclusions are as follows. We have presented two independent types of analysis, which allow a clear identification of coordination defects in *l*-Se, these defects being associated with onefold- and threefold-coordinated atoms (C_1 and C_3 defects). The C_1 and C_3 defects give rise to localized electronic states near the bottom and top of the band gap, respectively. The two types of analysis give essentially the same defect concentrations. These concentrations yield chain lengths that are much smaller (by a factor of ~15 at 870 K) than those deduced by Warren and Dupree from NMR measurements, and we suggest that only a small fraction of defects act as paramagnetic centers. Except near the melting point, defects fluctuate rapidly (on a time scale of less than 1 ps) between C_1 and C_3 character, and this fluctuation is closely related to the bond lifetime and the atomic diffusion. Our simulations give evidence for the importance of intimate valence alternation pairs (iVAPs) in the region of 570 K, but they become much less important at high temperature.

ACKNOWLEDGMENTS

The support of EPSRC through Grant Nos. GR/08946 and GR/L38592 is gratefully acknowledged.

---

*Present address: Institut für Theoretische Physik, Technische Universität Wien, Wiedner Hauptstrasse 8-10/136, A-1040 Wien, Austria.

†Present address: Dept. of Electrical Engineering, Ohio State University, Columbus, Ohio 43210.

[1] F. Kirchhoff, G. Kresse, and M. J. Gillan, Phys. Rev. B **57**, 10 482 (1998).

[2] V. M. Glazov, S. N. Chizhevskaya, and N. N. Glagoleva, *Liquid Semiconductors* (Plenum, New York, 1969).

[3] J. C. Perron, J. Rabit, and J. F. Rialland, Philos. Mag. B **46**, 321 (1982).

[4] K. Suzuki, Ber. Bunsenges. Phys. Chem. **80**, 689 (1976).

[5] M. Misawa and K. Suzuki, Trans. Jpn. Inst. Met. **18**, 427 (1977).

[6] R. Bellissent and G. Tourand, J. Non-Cryst. Solids **35-36**, 1221 (1980).

[7] M. Edeling and W. Freyland, Ber. Bunsenges. Phys. Chem. **85**, 1049 (1981).

[8] K. Tamura, J. Non-Cryst. Solids **117/118**, 450 (1990).

[9] K. Tamura and S. Hosokawa, Ber. Bunsenges. Phys. Chem. **96**, 681 (1992).

[10] M. Inui, T. Noda, K. Tamura, and C. Li, J. Phys.: Condens. Matter **8**, 9347 (1996).

[11] H. Hoshino, R. W. Schmutzler, W. W. Warren, and F. Hensel, Ber. Bunsenges. Phys. Chem. **80**, 27 (1976).

[12] S. Hosokawa and K. Tamura, J. Non-Cryst. Solids **117/118**, 52 (1990).

[13] S. Hosokawa and K. Tamura, J. Non-Cryst. Solids **117/118**, 489 (1990).

[14] F. J. DiSalvo, A. Menth, J. V. Waszaczak, and J. Tauc, Phys. Rev. B **6**, 4574 (1972).

[15] S. C. Agarwal, Phys. Rev. B **7**, 685 (1973).

[16] J. A. Gardner and M. Cutler, Phys. Rev. B **20**, 529 (1979).

[17] W. W. Warren and R. Dupree, Phys. Rev. B **22**, 2257 (1980).

[18] D. C. Koningsberger, J. H. M. C. van Wolput, and P. C. U. Rieter, Chem. Phys. Lett. **8**, 145 (1971).

[19] H. Hoshino, R. W. Schmutzler, W. W. Warren, and F. Hensel, Philos. Mag. **33**, 255 (1976).

[20] H.-P. Seyer, K. Tamura, H. Hoshino, H. Endo, and F. Hensel, Ber. Bunsenges. Phys. Chem. **90**, 587 (1986).

[21] H. Ikemoto, I. Yamamoto, and H. Endo, J. Non-Cryst. Solids **156-158**, 732 (1993).

[22] P. W. Anderson, Phys. Rev. Lett. **34**, 953 (1975).

[23] R. A. Street and M. F. Mott, Phys. Rev. Lett. **35**, 1293 (1975).

[24] M. Kastner, D. Adler, and H. Fritzsche, Phys. Rev. Lett. **37**, 1504 (1976).

[25] R. A. Street, Adv. Phys. **25**, 397 (1976).

[26] S. G. Bishop, U. Strom, and P. C. Taylor, Phys. Rev. Lett. **36**, 543 (1976); S. G. Bishop, U. Strom, and P. C. Taylor, Phys. Rev. B **15**, 2278 (1977).

[27] G. Kresse and J. Hafner, Phys. Rev. B **49**, 14 251 (1994).

[28] G. Kresse and J. Furthmüller, Comput. Mater. Sci. **6**, 15-50 (1996); G. Kresse and J. Furthmüller, Phys. Rev. B **54**, 11 169 (1996).

[29] Y. Wang and J. P. Perdew, Phys. Rev. B **44**, 13 298 (1991).

[30] W. H. Press, B. P. Flannery, S. A. Teukolsky, and W. T. Vetterling, *Numerical Recipes* (Cambridge University Press, New York, 1986).

[31] D. Hohl and R. O. Jones, Phys. Rev. B **43**, 3856 (1991).

[32] R. J. Bell and P. Dean, in *Amorphous Materials*, edited by R. W. Douglas and B. Ellis (Wiley, New York, 1972), p. 443.

[33] D. Vanderbilt and J. D. Joannopoulos, Phys. Rev. Lett. **42**, 1012 (1979).

[34] G. Kresse, J. Furthmüller, and J. Hafner, Phys. Rev. B **50**, 13 181 (1994).

[35] D. A. Drabold, P. A. Fedders, S. Klemm, and O. F. Sankey, Phys. Rev. Lett. **67**, 2179 (1991).

[36] I. Štich, M. Parrinello, and J. M. Holender, Phys. Rev. Lett. **76**, 2077 (1996).

[37] L. Hedin, Phys. Rev. **139**, A796 (1965).

[38] H. N. Rojas, R. W. Godby, and R. J. Needs, Phys. Rev. Lett. **74**, 1827 (1995).